

Med-SegLens: Latent-Level Model Differing for Interpretable Medical Image Segmentation

Salma J. Ahmed¹ Emad A. Mohammed¹ Azam Asilian Bidgoli¹

Abstract

Modern segmentation models achieve strong predictive performance but remain largely opaque, limiting our ability to diagnose failures, understand dataset shift, or intervene in a principled manner. We introduce **Med-SegLens**, a model-differing framework that decomposes segmentation model activations into interpretable latent features using sparse autoencoders trained on SegFormer and U-Net. Through cross-architecture and cross-dataset latent alignment across healthy, adult, pediatric, and sub-Saharan African glioma cohorts, we identify a stable backbone of shared representations, while dataset shift is driven by differential reliance on population-specific latents. We show that these latents act as causal bottlenecks for segmentation failures, and that targeted latent-level interventions can correct errors and improve cross-dataset adaption without retraining, recovering performance in 70% of failure cases and improving Dice score from 39.4% to 74.2%. Our results demonstrate that latent-level model differencing provides a practical and mechanistic tool for diagnosing failures and mitigating dataset shift in segmentation models.

1. Introduction

Medical image segmentation underpins computer-aided diagnosis, treatment planning, and disease monitoring (Pham et al., 2000). Despite strong benchmark performance from convolutional and transformer-based models (Sultana et al., 2020; Xiao et al., 2023; Litjens et al., 2017), their internal representations remain largely opaque. This limits our ability to diagnose systematic failures, understand dataset shifts, or intervene in a principled way, particularly in high-stakes clinical settings where models are deployed across heterogeneous populations (Holzinger et al., 2017).

¹Department of Physics and Computer Science, Wilfrid Laurier University, Waterloo, Canada. Correspondence to: Salma J. Ahmed <ahme3460@mylaurier.ca>.

Preprint. February 12, 2026.

Current mitigation strategies rely on retraining or post hoc interpretability methods (Selvaraju et al., 2017; Schlemper et al., 2019). While useful for visualization, these approaches provide limited causal insight into how internal representations encode population-specific priors or drive errors under distribution shift (Adebayo et al., 2018; Rudin, 2019). As a result, failures are difficult to attribute, compare across datasets, or correct without costly retraining.

We introduce **Med-SegLens**, a mechanistic *model-differing* framework for medical image segmentation that analyzes how internal representations differ across datasets Figure 1. Med-SegLens applies sparse autoencoders (SAEs) to intermediate activations of segmentation models, enabling a sparse, latent-level decomposition of learned features (Templeton et al., 2024; Gao et al., 2024). To ground these latents in the imaging domain, we propose a geometry- and spatially grounded automated interpretation pipeline that assigns anatomical and pathological semantics.

Our central contribution is a latent alignment and differencing procedure that decomposes representation shifts into *shared* and *dataset-specific* latent features. We show that dataset-specific latents act as causal bottlenecks for segmentation performance: intervening on them through targeted ablation or steering induces predictable changes in model behavior. Across multiple cohorts and architectures (SegFormer (Xie et al., 2021) and U-Net (Ronneberger et al., 2015)), this enables diagnosis and partial mitigation of segmentation failures *without retraining*, recovering performance in 70% of failure cases and improving Dice on the most affected failure class from 39.4% to 74.2%.

Our work suggests that population-specific priors in medical segmentation models are encoded in identifiable and manipulable latent features. Med-SegLens offers a principled framework for analyzing dataset shift and exploring representation-level interventions for segmentation failures. Our contributions are summarized as follows:

- We introduce **Med-SegLens**, the *first* mechanistic *model-differing* framework for medical image segmentation, enabling principled comparison of segmentation models across datasets via interpretable representations.
- We propose a geometry- and spatially grounded auto-

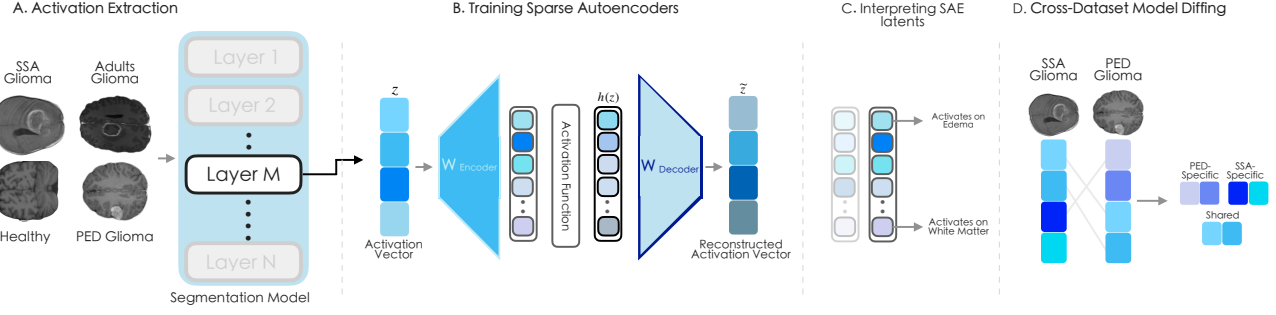


Figure 1. Overview of the proposed framework. We extract intermediate activations from a medical image segmentation model (A) and train sparse autoencoders on these activations to learn interpretable latent features (B). Using our Auto-Interp method, we assign semantic meaning to the learned latents (C). Finally, we perform cross-dataset model differencing to characterize domain shift and enable targeted latent-level interventions (D).

mated method for interpreting latent features.

- We show that cross-dataset model differencing reveals shared and population-specific latents, with the latter acting as causal bottlenecks under dataset shift.
- We demonstrate that segmentation failures can be traced to individual latents and mitigated through targeted interventions, recovering performance in 70% of failure cases.
- Without retraining, we improve cross-dataset adaptation by mitigating class-specific bias, increasing Dice from 39.4% to 74.2% on the most affected class.

2. Related Work

Our work bridges mechanistic interpretability, model differencing, and medical image segmentation by using Sparse autoencoders to extract interpretable latent representations and the Hungarian algorithm to analyze cross-dataset representation shift.

Interpretability in Medical Image Segmentation Most interpretability approaches for medical image segmentation rely on post hoc saliency or attention-based techniques, such as SHAP and Grad-CAM and its variants (Selvaraju et al., 2017; Lundberg & Lee, 2017; Schlemper et al., 2019). While these methods highlight regions correlated with predictions, they do not reveal the internal representations driving segmentation decisions, explain failures under dataset shift, or enable principled error diagnosis or control (Rudin, 2019).

Mechanistic Interpretability aims to explain neural network behavior by reverse-engineering models to identify the algorithms, features, and circuits they implement (Olah et al., 2017; Elhage et al., 2022). Recent work has made substantial progress in identifying task-relevant circuits in language models (Nanda et al., 2023; Olah et al., 2020; Cunningham et al., 2023) and in vision models, primarily for

classification backbones such as ViTs/CLIP (Dosovitskiy, 2020; Achitabat et al., 2022; Gandelsman et al., 2024; 2023; Komorowski et al., 2023; Zaigrajew et al., 2025). However, analogous mechanistic analyses for dense prediction tasks such as medical image segmentation remain largely unexplored. We extend mechanistic interpretability to segmentation by uncovering how models represent anatomical structure, why failures arise under dataset shift, and how targeted latent interventions can correct these failures.

Model Differencing and Dataset Shift aims to identify changes in the internal representations of two models. Methods such as CrossCoders (Lindsey et al., 2024) have been used to analyze representation differences in language models, including risks and fine-tuning side effects (Kassem et al., 2025; Minder et al., 2025; Boughorbel et al., 2025; Wang et al., 2025; Jiralerpong & Bricken). The Hungarian algorithm has also been proposed for model alignment (Paulo & Belrose, 2025). However, applying model differencing to study dataset shift or cross-dataset representation learning remains largely underexplored in segmentation models. We apply model differencing to models trained on different datasets to characterize representation shift and adaptation.

3. Background and Methods

3.1. Problem Setting: Representation-Level Model Differing

Our goal is to understand how segmentation models differ internally when trained on distinct medical populations, and how these differences relate to systematic failures under dataset shift. Rather than analyzing a single model in isolation, we adopt a *model differencing* perspective: given two segmentation models trained on different datasets but sharing the same architecture, we explicitly compare their internal representations to identify (i) shared, population-invariant features and (ii) dataset-specific features that act as causal bottlenecks for performance (Algorithm 1).

Formally, let $f_{\theta(d)} : \mathcal{X} \rightarrow \mathcal{Y}$ denote a segmentation model trained on dataset d . Given two datasets d_1, d_2 , our objective is to characterize differences in the internal feature spaces of $f_{\theta(d_1)}$ and $f_{\theta(d_2)}$ at the level of interpretable latent components, rather than raw activations or output predictions.

3.2. Population Knowledge and Datasets

Datasets. We study representation shift across brain MRI datasets spanning distinct populations and pathologies. Healthy anatomy is represented by the IXI dataset (Consortium, 2012), while pathological domains are drawn from the BraTS 2023 challenge (Menze et al., 2014; Baid et al., 2021), including adult glioma, pediatric glioma, and sub-Saharan African (SSA) glioma cohorts. We use a preprocessed version of IXI (Chen et al., 2022) with voxel-level subcortical segmentation masks, mapping the original anatomical labels to a reduced set of target classes.

Although all datasets consist of T1-weighted brain MRIs, they differ substantially in population demographics, disease presentation, and acquisition distributions, making them well-suited for studying population-specific versus shared representations. Additional statistical details are provided in Appendix A.

3.3. Controlled Model Training

To isolate representation differences due solely to data, we train the *same segmentation architecture independently* on each dataset. We experiment with SegFormer-B4, a Transformer-based model, and U-Net as a convolutional baseline. With four tumor classes for BraTS cohorts and nine anatomical classes for IXI.

All input images are resized to 256×256 . Training uses standard data augmentation, while validation uses deterministic preprocessing. This results in four dataset-specific models:

$$\{f_{\theta(\text{Adult})}, f_{\theta(\text{PED})}, f_{\theta(\text{SSA})}, f_{\theta(\text{IXI})}\},$$

which form the basis for all subsequent model-differing analyses.

3.4. Latent Extraction with Sparse Autoencoders

Directly differencing raw activations is challenging due to their high dimensionality and lack of semantic structure. To obtain a disentangled and comparable representation space, we decompose internal activations using sparse autoencoders (SAEs).

For each trained segmentation model, we extract activations from a fixed intermediate layer¹ and train a BatchTopK

¹We select a middle layer, as prior work shows it captures the richest semantic structure (Skean et al., 2025) Appendix B.

Algorithm 1 Latent-Level Model Differing for Segmentation

Require: Datasets $\{\mathcal{D}_m\}_{m=1}^M$, architecture f_θ , sparsity k , threshold τ
Ensure: Shared and dataset-specific latent features

- 1: **for** each dataset \mathcal{D}_m **do**
- 2: Train segmentation model $f_{\theta(m)}$ on \mathcal{D}_m
- 3: Extract intermediate activations $X^{(m)}$
- 4: Train BatchTopK SAE on $X^{(m)}$
- 5: Obtain encoder and decoder weights
- 6: **end for**
- 7: **for** each dataset pair (m, n) **do**
- 8: **for** $p \in \{\text{enc, dec}\}$ **do**
- 9: Compute cosine similarity matrix C^p
- 10: Compute matching π^p using Hungarian algorithm
- 11: **end for**
- 12: Identify shared latent indices satisfying:
- 13: $\pi^{\text{enc}}(i) = \pi^{\text{dec}}(i)$
- 14: $C_{i, \pi(i)}^{\text{enc}} \geq \tau$ and $C_{i, \pi(i)}^{\text{dec}} \geq \tau$
- 15: **end for**

sparse autoencoder (Bussmann et al., 2024) (Figure 1A-B). Given a batch of activations $X \in \mathbb{R}^{n \times d}$, the SAE computes

$$Z = \text{BatchTopK}(XW_{\text{enc}} + b_{\text{enc}}), \quad \hat{X} = ZW_{\text{dec}} + b_{\text{dec}},$$

where $Z \in \mathbb{R}^{n \times m}$ is a sparse latent representation. The BatchTopK operator retains the top $n \times k$ activations across the batch, enforcing an average sparsity of k active latents per sample while allowing adaptive allocation based on sample complexity.

The SAE is trained using reconstruction loss

$$\mathcal{L}_{\text{SAE}} = \|X - \hat{X}\|_2^2.$$

We set $k = 32$ and use an expansion factor of 16. Smaller expansion factors produced broader, less interpretable features, while larger expansions encouraged feature splitting and yielded more monosemantic latents (Bricken et al., 2023) (subsection B.2). Each dataset thus yields an SAE whose latent dimensions serve as the atomic units for model differing.

3.5. Automated Latent Semantics Discovery

To interpret SAE latents, we analyze their Top- K highest-activating samples and corresponding spatial activation maps (Figure 1C). For each latent z_i , we generate activation heatmaps by projecting latent activations back to the spatial resolution of the segmentation model and overlay them on the input image and ground-truth mask.

We further introduce an automated interpretation pipeline that maps latent activations to structured anatomical semantics. For each latent, we compute geometry- and spatial-based metrics, including brain-edge ratio, depth within brain

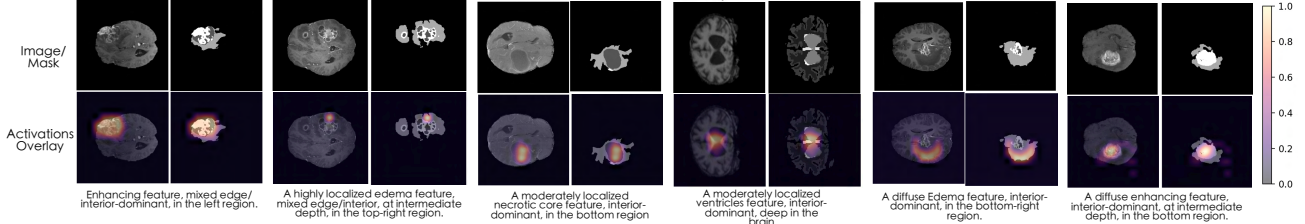


Figure 2. Examples of SAE features from Segformer and UNET. Shown are representative SAE latents corresponding to tumor subregions (edema, enhancing tumor, and necrotic core), capturing diverse spatial and morphological patterns, alongside features associated with healthy anatomy. Each latent is accompanied by its auto-interpreted semantic description. The top row shows the MRI image and ground-truth mask, and the bottom row visualizes the SAE activation heatmap overlaid on the MRI and segmentation mask.

tissue, spatial entropy, and centroid localization. These metrics provide quantitative descriptors of *where* and *how* a latent activates (Further Details [Appendix C](#)).

Latents are interpreted in a dataset-specific context: for BraTS, we assess alignment with tumor subregions (edema, enhancing tumor, necrotic core), while for IXI we analyze correspondence with healthy anatomical structures such as white matter, gray matter, and ventricles. This step grounds latent features in clinically meaningful concepts and enables principled comparison across datasets.

3.6. Cross-Dataset Model Differing via Latent Alignment

Our core contribution is a latent-level model differing procedure that explicitly aligns sparse autoencoder (SAE) features across datasets. Because SAE latent indices are arbitrary, direct comparison requires solving a feature correspondence problem ([Figure 1D](#)).

Given two SAEs trained on datasets d_1 and d_2 , with encoder and decoder weights $W_{\text{enc}}^{(1)}, W_{\text{dec}}^{(1)}$ and $W_{\text{enc}}^{(2)}, W_{\text{dec}}^{(2)}$, we compute cosine similarity matrices between corresponding latent vectors:

$$C_{ij}^p = \cos(W_{p,i}^{(1)}, W_{p,j}^{(2)}), \quad p \in \{\text{enc, dec}\}.$$

To obtain a strict one-to-one correspondence between latents, we apply the Hungarian algorithm to each similarity matrix, yielding matchings

$$\pi^p = \text{Hungarian}(C^p), \quad p \in \{\text{enc, dec}\}.$$

We define the set of *shared* latents as

$$\mathcal{S} = \left\{ i \mid \pi^{\text{enc}}(i) = \pi^{\text{dec}}(i), C_{i,\pi(i)}^{\text{enc}} \geq \tau, C_{i,\pi(i)}^{\text{dec}} \geq \tau \right\},$$

where τ is a similarity threshold. We set $\tau = 0.8$, selected via a sweep as the value that best balances stability and coverage. Latents outside \mathcal{S} are classified as dataset-specific.

This conservative criterion isolates a stable backbone of population-invariant representations while identifying dataset-specific latents that differ systematically across models. The resulting alignment underpins our downstream

analyses of representation shift, failure diagnosis, and latent intervention.

4. Latent Feature Analysis

4.1. SAEs Uncover Interpretable Features

Our automated interpretation framework reveals that sparse autoencoders decompose segmentation model activations into a set of semantically meaningful latent features. These latents capture both generic visual patterns, such as background structure and edge-related information, as well as domain-specific concepts corresponding to tumor subregions and healthy anatomical structures.

[Figure 2](#) shows representative SAE latents and activation heatmaps from both U-Net and SegFormer. Together with automatically generated semantic labels, these results demonstrate that individual latents align with distinct visual and anatomical concepts, consistently across architectures and datasets. Rather than a single latent per class, multiple latents emerge for each tumor or anatomical category, capturing variation in spatial location, morphology (e.g., diffuse vs. localized), scale, and depth within the brain ([Appendix D](#)). This decomposition shows that SAEs disentangle fine-grained, clinically relevant structure, encoding tumors not only by presence but by diverse, appearance-dependent features.

As a sanity check, we evaluate the method on a non-medical dataset, showing it captures meaningful structure despite differing visual statistics and semantics ([Appendix F](#)).

4.2. Cross-Architecture Internal Reasoning

We compare how SegFormer and U-Net utilize internal representations by analyzing SAE latent activations under identical training and inference conditions. Using 100 BraTS-Adult cases, we aggregate activation mass per latent and group features into tumor, background, and boundary categories.

As shown in [Figure 3](#), both models are dominated by background features, reflecting the prevalence of non-tumor

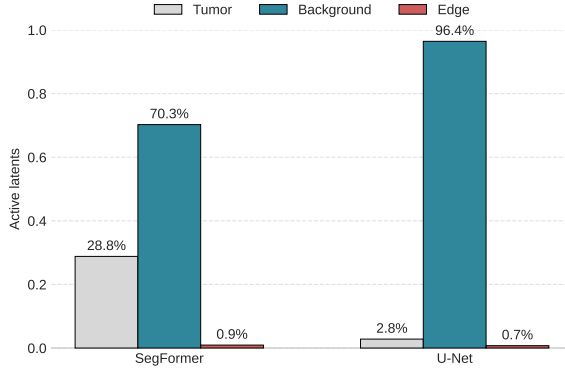


Figure 3. Distribution of active SAE latents across semantic categories for SegFormer and UNet on 100 BraTS-Adult cases, grouped by automated semantic interpretation.

Table 1. Fraction of shared SAE latents of SegFormer trained on different dataset cohorts.

Dataset Pair	Shared Latents (%)
Adult Glioma \leftrightarrow Pediatric Glioma	58.9
Adult Glioma \leftrightarrow Sub-Saharan Glioma	43.2
Adult Glioma \leftrightarrow Healthy Brains	36.1

anatomy in MRI. However, latent usage differs sharply: UNet relies almost exclusively on background latents (Tumor: 2.8%), while SegFormer activates substantially more tumor-related latents (Tumor: 28.8%), yielding a more balanced representation and highlighting clear architectural differences in internal feature utilization.

5. Do Models Learn Shared Representations Across Datasets?

A central question in medical image segmentation is whether models trained on different populations learn shared internal representations or diverge under dataset shift. Although all datasets depict the same organ (the brain), they differ substantially in acquisition protocols, demographics, and disease prevalence.

We study four domains healthy adults, adult glioma, pediatric glioma (PED), and Sub-Saharan African (SSA) glioma and train the same architecture independently on each using matched optimization settings, isolating the effect of data distribution on learned representations.

5.1. Model Differing via Sparse Autoencoders

We analyze representation differences across datasets using our *latent-level model differing framework* based on sparse autoencoders (SAEs). SAEs provide an interpretable latent basis that enables direct, feature-level comparison between independently trained segmentation models.

5.2. Shared and Dataset-Specific Representations

Table 1 reports the fraction of shared latents between dataset pairs. All pairs show non-zero overlap, indicating a partially shared internal basis across populations. Adult–pediatric models share the most latents, followed by adult–SSA and adult–healthy (see Appendix E for additional pairs). Shared representations are more prevalent among diseased cohorts than between diseased and healthy data, consistent with tumor-specific structure. The lower overlap with SSA likely reflects domain shift from scanner and image-quality differences (Adewole et al., 2023). Overall, these results show that segmentation models learn both population-invariant and dataset-specific representations, explaining cross-dataset generalization and failures under distribution shift.

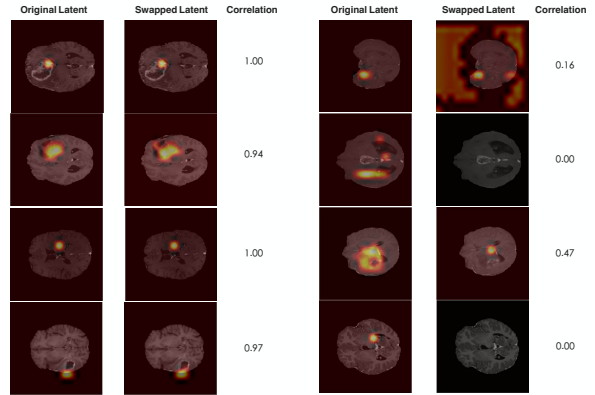


Figure 4. Feature swapping between Adult and Pediatric SAEs. Shared latents (left) preserve activation structure and spatial correlation, while non-shared latents (right) produce disrupted or absent activations.

5.3. Causal Role of Shared Latents

We test the causal role of shared latents via *feature swapping* between SAEs trained on Adult and Pediatric data. Let $h \in \mathbb{R}^d$ denote activations from a fixed model layer. An SAE trained on dataset $D \in \{\text{Adult, Pediatric}\}$ encodes and reconstructs

$$z^{(D)} = W_{\text{enc}}^{(D)} h, \quad \hat{h}^{(D)} = W_{\text{dec}}^{(D)} z^{(D)}.$$

Given aligned latent indices \mathcal{I} , we swap shared components:

$$\tilde{z}_i^{(\text{Adult})} = \begin{cases} z_i^{(\text{Pediatric})}, & i \in \mathcal{I}, \\ z_i^{(\text{Adult})}, & \text{otherwise.} \end{cases}$$

The modified activation is

$$\tilde{h} = W_{\text{dec}}^{(\text{Adult})} \tilde{z}^{(\text{Adult})},$$

which is propagated through the remaining network with all weights fixed.

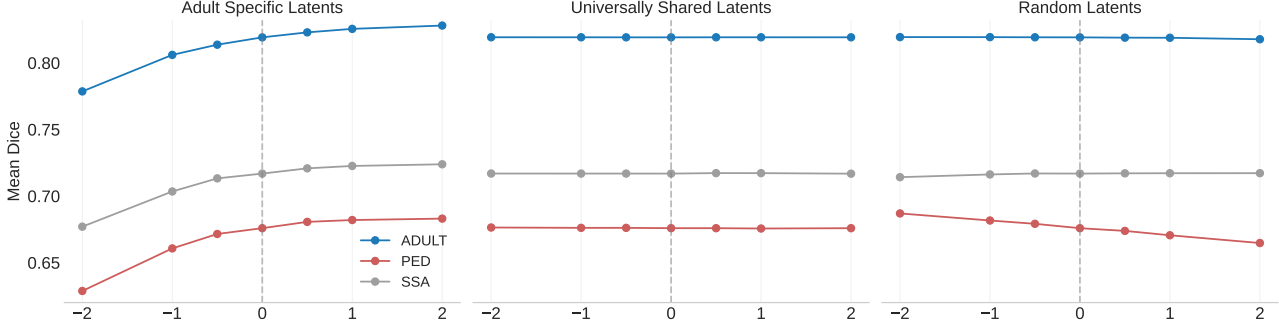


Figure 5. Mean Dice versus steering strength (α) for adult-specific (left), universally shared (middle), and random (right) SAE latents. Adult-specific steering strongly affects Adult performance and weakly affects Pediatric and SSA, while shared or random steering yields minimal, non-selective changes.

As shown in Figure 4, swapping shared latents preserves spatial localization and semantic structure, with high correlation to original activations, indicating domain-invariant representations. In contrast, swapping non-shared latents yields diffuse or inactive responses and low correlation, reflecting domain-specific features. These results provide causal evidence that encoder–decoder aligned latents act as transferable mechanisms, while non-aligned latents do not (see Appendix E).

5.4. Universally Shared Latents

Beyond pairwise overlap, we examine whether *universally shared* latents exist—features identified as shared across all dataset pairs. Let $\mathcal{S}_{m,n}$ denote shared latents between datasets m and n ; universally shared latents are

$$\mathcal{S}_{\text{univ}} = \bigcap_{m \neq n} \mathcal{S}_{m,n}.$$

All remaining latents are treated as population-specific.

To assess their role, we steer an Adult-trained SegFormer and evaluate on Adult, Pediatric, and SSA data. Steering population-specific latents strongly affects in-domain performance but has weaker out-of-domain effects (Figure 5), indicating population-aligned causal bottlenecks. In contrast, steering universally shared latents yields minimal changes across datasets, comparable to random steering. Inspection via automated interpretation reveals that these universally shared latents predominantly encode stable anatomical, background, and boundary features, explaining their limited impact on tumor segmentation. Together, these results indicate that dataset shift arises from population-specific latent circuits rather than mismatched shared representations.

5.5. Baselines Comparison

We compare our cross-dataset latent differencing method against three baselines, Greedy matching, Sinkhorn alignment, and encoder-only Hungarian matching using four unsupervised metrics: *Agreement*, the fraction of latents whose matches

Table 2. Unsupervised comparison of latent alignment methods between adults and pediatrics datasets.

Method	Agreement \uparrow	Stability \uparrow	Collision \downarrow	Predictability \uparrow
Greedy	98.0	98.5	0.014	78.7
Sinkhorn	98.9	99.4	0.006	78.6
Enc-only	99.0	98.9	0.000	78.5
Ours	100.0	100.0	0.000	90.0

agree between encoder- and decoder-based alignment; *Stability*, robustness under bootstrap resampling of the SAE dictionaries; *Collision*, the rate of many-to-one assignments; and *Predictability*, a functional specificity score measuring the gap between aligned similarity and a shuffled baseline (see subsection E.1). We do not use CrossCoder-based alignment due to known limitations: CrossCoders learn a shared projection that can entangle shared and model-specific features and exhibit instability across runs, which complicates correspondence interpretation (Mishra-Sharma et al., 2024; Dumas et al., 2025).

As shown in Table 2, *Agreement* and *Stability* are high for all methods, indicating that cross-dataset SAE alignment is well-conditioned. While Greedy, Sinkhorn, and encoder-only Hungarian recover largely consistent matches, they rely on a single projection space. Our method enforces cross-space consistency, yielding perfect agreement and substantially higher *Predictability*, indicating more specific and non-accidental correspondence.

6. Failure Diagnosis and Latent Intervention

We analyze whether segmentation failures can be diagnosed and corrected through representation-level analysis, focusing on instance-level and class-level weaknesses in SegFormer. We contextualize our approach using widely adopted inference-level refinements in BraTS pipelines, including connected-component (CCF) post-processing (Menze et al., 2014; Rai et al., 2024) and entropy-based uncertainty filtering (UF) from the BraTS uncertainty challenge (Mehta et al., 2022; Mehrtash et al., 2020). These methods suppress spurious or low-confidence predictions

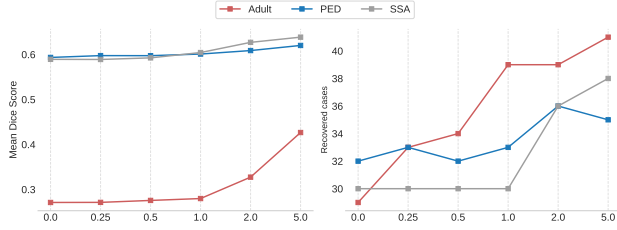


Figure 6. Effect of steering the most activated latent on failure cases across Pediatric (PED), Sub-Saharan African (SSA), and Adult glioma datasets. Amplifying these latents with increasing scaling strength improves the mean Dice score and increases the number of recovered cases.

Table 3. Mean Dice (%) on failure cases across datasets. We report absolute performance and improvement over the base model (Δ).

Intervention	Adult	PED	SSA
Base Model	25.3	58.8	59.2
CCF	25.7 (+0.4)	47.4 (-11.4)	55.7 (-3.5)
UF	27.5 (+2.2)	47.5 (-11.3)	56.4 (-2.8)
Ours	43.0 (+17.7)	62.0 (+3.2)	63.8 (+4.6)

and provide complementary points of comparison to our internal, causal interventions.

6.1. Instance-Level Failure Diagnosis

For each BraTS Adult, Pediatric, and Sub-Saharan African (SSA) dataset, we analyze the 60 lowest-performing cases as failure instances, selected to balance stability and specificity. For each case, we examine the top- K most active sparse autoencoder (SAE) latents and observe systematic deviations in latent usage, with some latents abnormally amplified or suppressed.

Latent Steering for Failure Recovery. To test whether failures arise from latent miscalibration, we intervene on the most active SAE latents via latent steering. Given a latent vector \mathbf{z} and selected indices \mathcal{K} , activations are scaled as

$$\tilde{z}_i = \begin{cases} \alpha z_i, & i \in \mathcal{K}, \\ z_i, & \text{otherwise,} \end{cases}$$

with $\alpha \in \{0.25, 0.5, 1.0, 2.0, 5.0\}$. As shown in Figure 6, increasing α recovers performance in 70.6%, 60.0%, and 63.3% of failure cases for Adult, Pediatric, and SSA datasets, respectively, substantially improving mean Dice without retraining.

Comparison with Baselines. Connected-component and entropy-based uncertainty filtering provide only modest gains, improving some Adult cases but failing to recover most Pediatric and SSA failures (Table 3). This reflects their

nature, which suppresses false positives but does not restore missing structure.

Interpreting Corrective Latents. Automated interpretation shows that corrective latents predominantly encode background-related features; amplifying them suppresses spurious tumor responses. Such representation-level corrections are inaccessible to output-level baselines.

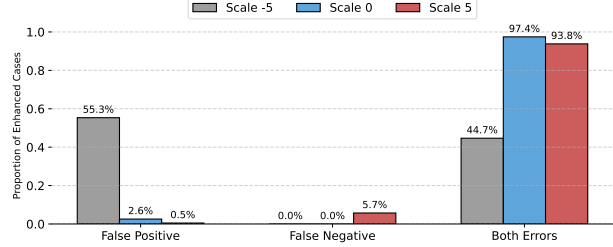


Figure 7. Failure-mode-specific effects of edema latent steering. Suppression primarily corrects false positives, amplification recovers false negatives, and both improve mixed-error cases, demonstrating complementary causal interventions.

6.2. Class-Level Performance Disparities

Beyond instance-level failures, the Adult model exhibits a systematic class-specific weakness: edema achieves a mean Dice of 65%, compared to 80% for enhancing tumor and 81% for necrotic core. We therefore focus on Adult cases with edema Dice below 50% (2,844 cases).

Class-Specific Latent Intervention. Using model differing and automated interpretation, we identify edema-related latents and apply targeted steering via amplification, suppression, and zeroing (Figure 7). Error analysis reveals three dominant modes: false positives, false negatives, and mixed errors with suppression correcting hallucinations, amplification recovering missing edema, and zeroing best handling mixed cases.

Across the 2,844 failures, latent intervention recovers 1,344 cases (47.25%), improving edema Dice from 65% to 69% and overall mean Dice from 81.8% to 82.6 without retraining. Baselines provide limited benefit on this subset (Table 4), as many failures are false-negative-dominated and require restoring missing internal features rather than suppressing uncertain predictions.

Table 4. Edema and mean Dice (%) on Adult failure cases. Absolute scores and improvement over the base model (Δ) are reported.

Intervention	Edema Dice	Mean Dice
Base Model	65.8	81.8
CCF	65.6 (-0.2)	81.7 (-0.09)
UF	65.8 (+0.0)	81.8 (+0.0)
Ours	69.1 (+3.2)	82.6 (+0.79)

Table 5. Cross-domain segmentation performance between Adult and Pediatric cohorts, reporting per-class Dice (Classes 1–3), mean Dice, and edema precision (PR) and recall (RR), with absolute scores and improvement over baseline (Δ).

Method	Adult → Pediatrics					Pediatrics → Adult				
	Necrotic	Edema	Enhancing	Mean Dice	PR	Necrotic	Edema	Enhancing	Mean Dice	RR
Base Model	59.6	39.4	72.5	67.8	22.2	59.5	45.2	78.3	70.6	35.3
CCF	48.6 (-11)	60.0 (+20)	69.1 (-3)	69.3 (+1)	26.2 (+4)	52.9 (-6)	22.0 (-23)	45.3 (-33)	54.7 (-15)	0.02 (-35)
UF	59.6 (+0)	39.6 (+.2)	73.2 (+.7)	68.0 (+.2)	22.4 (+.2)	59.7 (+.2)	45.1 (-.1)	78.3 (+0)	70.6 (+0)	35.1 (-.2)
ALS (Ours)	57.5 (-2)	74.2 (+34)	76.1 (+3)	76.9 (+9)	73.7 (+51)	55.0 (-4)	49.3 (+4)	73.3 (-5)	69.2 (-1)	48.5 (+13)
MLS (Ours)	58.8 (-.8)	52.3 (+12)	71.8 (-.7)	70.6 (+2)	29.1 (+6)	59.8 (+.3)	48.5 (+3)	77.8 (-.5)	71.4 (+.8)	42.3 (+7)

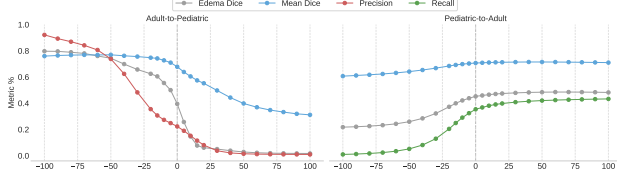


Figure 8. Domain adaptation under OOD shift. Negative scaling improves Adult→Pediatric performance, while positive scaling improves Pediatric→Adult performance, particularly for edema.

7. Out-of-Distribution Adaptation Without Retraining

Using model diffing, we separate domain-invariant SAE latents from population-specific latents, which act as causal bottlenecks under distribution shift. We study a realistic deployment setting: adapting a single trained segmentation model to out-of-distribution data *without retraining or access to target-domain models*. We evaluate two latent intervention strategies (Rimsky et al., 2024; Turner et al., 2023).

Additive Latent Steering (ALS). We inject a constant offset into selected SAE latents,

$$z_k \leftarrow z_k + \alpha, \quad k \in \mathcal{K}.$$

Multiplicative Latent Steering (MLS). We rescale selected latents,

$$z_k \leftarrow \alpha z_k, \quad k \in \mathcal{K},$$

modulating feature strength without introducing new signals.

We sweep $\alpha \in [-100, 100]$. We evaluate Adult→Pediatric and Pediatric→Adult adaptation, where performance degradation is consistently dominated by the edema class (Table 5). Using automated latent interpretation, we identify edema-controlling SAE latents and intervene on them at inference time.

The optimal strategy depends on adaptation direction. ALS is most effective for Adult→Pediatric, while MLS performs best for Pediatric→Adult (Figure 8). Adult→Pediatric errors are false-positive-dominated; suppressing edema

latents improves Class 2 Dice from 39% to $\sim 74\%$. Pediatric→Adult errors are false-negative-dominated; amplifying the same latents restores missing predictions, improving Dice, mean Dice, and recall.

As shown in Table 5, Connected-component filtering partially mitigates false positives in Adult→Pediatric adaptation (60%), but underperforms latent steering (74.2%). Uncertainty filtering yields minimal gains. In Pediatric→Adult, neither baseline recovers false negatives, whereas latent amplification succeeds.

8. Conclusion

We introduced a latent-level model diffing framework for medical image segmentation that enables direct comparison of internal representations across populations, revealing a clear separation between shared, population-invariant features and dataset-specific latent circuits that act as causal bottlenecks under distribution shift. By decomposing model activations with sparse autoencoders and aligning latents across independently trained models, we showed that systematic failures and cross-dataset performance gaps arise primarily from differential reliance on population-specific latents rather than a lack of shared representations, and that targeted latent-level interventions can recover failures, correct class-level disparities, and adapt models to out-of-distribution data without retraining or access to target-domain models. However, the latent features learned by SAEs are inherently sensitive to the training data distribution; although we analyze multiple cohorts spanning healthy anatomy and diverse tumor populations, different datasets may induce distinct or additional latent feature sets. Moreover, latent interpretation is constrained by the spatial and geometric metrics employed and the availability of ground-truth masks, meaning that latents with complex, diffuse, or overlapping activation patterns may be only partially or imperfectly interpreted. Future work will explore richer alignment strategies that support graded or many-to-many correspondences, improved attribution of dataset-specific latents, and more expressive interpretation mechanisms that reduce reliance on handcrafted metrics and annotations.

Impact Statement

This work introduces a mechanistic framework for analyzing and intervening on medical image segmentation models through latent-level model diffing. By decomposing internal representations into interpretable, population-aligned features, our approach enables systematic diagnosis of representation shift, identification of population-specific failure modes, and targeted correction of errors without re-training. The primary positive impact of this work lies in improving the reliability and equity of segmentation models under dataset and population shift. Our results show that performance degradation in underrepresented or out-of-distribution cohorts can often be traced to specific latent circuits and mitigated through causal interventions at inference time. This has the potential to reduce disparities in model performance across populations, particularly in settings where collecting large, representative datasets or re-training models is infeasible. Beyond medical imaging, the proposed framework contributes a general methodology for mechanistic model comparison and failure analysis, which may be applicable to other high-dimensional perception models. At the same time, we emphasize that these techniques are intended to support model auditing, robustness analysis, and scientific understanding, rather than to replace clinical judgment. Any deployment in high-stakes clinical environments requires rigorous validation, regulatory approval, and expert oversight.

References

Achitbat, R., Dreyer, M., Eisenbraun, I., Bosse, S., Wiegand, T., Samek, W., and Lapuschkin, S. From “where” to “what”: Towards human-understandable explanations through concept relevance propagation. *arXiv preprint arXiv:2206.03208*, 3, 2022.

Adebayo, J., Gilmer, J., Muelly, M., Goodfellow, I., Hardt, M., and Kim, B. Sanity checks for saliency maps. *Advances in neural information processing systems*, 31, 2018.

Adewole, M., Rudie, J. D., Gbdamosi, A., Toyobo, O., Raymond, C., Zhang, D., Omidiji, O., Akinola, R., Suwaid, M. A., Emegoakor, A., et al. The brain tumor segmentation (brats) challenge 2023: Glioma segmentation in sub-saharan africa patient population (brats-africa). *ArXiv*, pp. arXiv–2305, 2023.

Baid, U., Ghodasara, S., Mohan, S., Bilello, M., Calabrese, E., Colak, E., Farahani, K., Kalpathy-Cramer, J., Kitamura, F. C., Pati, S., et al. The rsna-asnr-miccai brats 2021 benchmark on brain tumor segmentation and radio-genomic classification. *arXiv preprint arXiv:2107.02314*, 2021.

Boughorbel, S., Dalvi, F., Durrani, N., and Hawasly, M. Beyond the leaderboard: Understanding performance disparities in large language models via model diffing. In *Proceedings of the 2025 Conference on Empirical Methods in Natural Language Processing*, pp. 31348–31359, 2025.

Bricken, T., Templeton, A., Batson, J., Chen, B., Jermyn, A., Conerly, T., Turner, N., Anil, C., Denison, C., Askell, A., Lasenby, R., Wu, Y., Kravec, S., Schiefer, N., Maxwell, T., Joseph, N., Hatfield-Dodds, Z., Tamkin, A., Nguyen, K., McLean, B., Burke, J. E., Hume, T., Carter, S., Henighan, T., and Olah, C. Towards monosemanticity: Decomposing language models with dictionary learning. *Transformer Circuits Thread*, 2023. URL <https://transformer-circuits.pub/2023/monosemantic-features/index.html>.

Bussmann, B., Leask, P., and Nanda, N. Batchtopk sparse autoencoders. *arXiv preprint arXiv:2412.06410*, 2024.

Chen, J., Frey, E. C., He, Y., Segars, W. P., Li, Y., and Du, Y. Transmorph: Transformer for unsupervised medical image registration. *Medical Image Analysis*, 2022.

Consortium, I. Ixi dataset: Information extraction from images. *Transformer Circuits Thread*, 2012. URL <https://brain-development.org/ixi-dataset/>.

Cunningham, H., Ewart, A., Riggs, L., Huben, R., and Sharkey, L. Sparse autoencoders find highly interpretable features in language models. *arXiv preprint arXiv:2309.08600*, 2023.

Dosovitskiy, A. An image is worth 16x16 words: Transformers for image recognition at scale. *arXiv preprint arXiv:2010.11929*, 2020.

Dumas, C., Minder, J., and Nanda, N. What we learned trying to diff base and chat models (and why it matters). AI Alignment Forum, 2025. URL <https://www.alignmentforum.org/posts/xmpauEXEerzYcJKNm/what-we-learned-trying-to-diff-base-and-chat-models-and-why-it-matters>.

Elhage, N., Hume, T., Olsson, C., Schiefer, N., Henighan, T., Kravec, S., Hatfield-Dodds, Z., Lasenby, R., Drain, D., Chen, C., et al. Toy models of superposition. *arXiv preprint arXiv:2209.10652*, 2022.

Fortin, J.-P., Parker, D., Tunç, B., Watanabe, T., Elliott, M. A., Ruparel, K., Roalf, D. R., Satterthwaite, T. D., Gur, R. C., Gur, R. E., et al. Harmonization of multi-site diffusion tensor imaging data. *Neuroimage*, 161:149–170, 2017.

Gandelsman, Y., Efros, A. A., and Steinhardt, J. Interpreting clip’s image representation via text-based decomposition. *arXiv preprint arXiv:2310.05916*, 2023.

Gandelsman, Y., Efros, A. A., and Steinhardt, J. Interpreting the second-order effects of neurons in clip. *arXiv preprint arXiv:2406.04341*, 2024.

Gao, L., la Tour, T. D., Tillman, H., Goh, G., Troll, R., Radford, A., Sutskever, I., Leike, J., and Wu, J. Scaling and evaluating sparse autoencoders. *arXiv preprint arXiv:2406.04093*, 2024.

Holzinger, A., Biemann, C., Pattichis, C. S., and Kell, D. B. What do we need to build explainable ai systems for the medical domain? *arXiv preprint arXiv:1712.09923*, 2017.

Jiralerspong, T. and Bricken, T. Cross-architecture model diffing with crosscoders: Unsupervised discovery of differences between llms. In *Mechanistic Interpretability Workshop at NeurIPS 2025*.

Kassem, A. M., Shi, Z., Rostamzadeh, N., and Farnadi, G. Reviving your mneme: Predicting the side effects of llm unlearning and fine-tuning via sparse model diffing. In *Proceedings of the 2025 Conference on Empirical Methods in Natural Language Processing*, pp. 32238–32251, 2025.

Komorowski, P., Baniecki, H., and Biecek, P. Towards evaluating explanations of vision transformers for medical imaging. In *Proceedings of the IEEE/CVF conference on computer vision and pattern recognition*, pp. 3726–3732, 2023.

Lee, C.-H., Liu, Z., Wu, L., and Luo, P. Maskgan: Towards diverse and interactive facial image manipulation. In *IEEE Conference on Computer Vision and Pattern Recognition (CVPR)*, 2020.

Lindsey, J., Templeton, A., Marcus, J., Conerly, T., Batson, J., and Olah, C. Sparse crosscoders for cross-layer features and model diffing. *Transformer Circuits Thread*, 2024. URL <http://transformer-circuits.pub/2024/crosscoders/index.html>.

Litjens, G., Kooi, T., Bejnordi, B. E., Setio, A. A. A., Ciompi, F., Ghafoorian, M., Van Der Laak, J. A., Van Ginneken, B., and Sánchez, C. I. A survey on deep learning in medical image analysis. *Medical image analysis*, 42: 60–88, 2017.

Lundberg, S. M. and Lee, S.-I. A unified approach to interpreting model predictions. *Advances in neural information processing systems*, 30, 2017.

Mehrtash, A., Wells, W. M., Tempany, C. M., Abolmaesumi, P., and Kapur, T. Confidence calibration and predictive uncertainty estimation for deep medical image segmentation. *IEEE transactions on medical imaging*, 39(12): 3868–3878, 2020.

Mehta, R., Filos, A., Baid, U., Sako, C., McKinley, R., Rebsamen, M., Dätwyler, K., Meier, R., Radojewski, P., Murugesan, G. K., et al. Qu-brats: Miccai brats 2020 challenge on quantifying uncertainty in brain tumor segmentation-analysis of ranking scores and benchmarking results. *The journal of machine learning for biomedical imaging*, 2022:https–www, 2022.

Menze, B. H., Jakab, A., Bauer, S., Kalpathy-Cramer, J., Farahani, K., Kirby, J., Burren, Y., Porz, N., Slotboom, J., Wiest, R., et al. The multimodal brain tumor image segmentation benchmark (brats). *IEEE transactions on medical imaging*, 34(10):1993–2024, 2014.

Minder, J., Dumas, C., Chughtai, B., and Nanda, N. Robustly identifying concepts introduced during chat fine-tuning using crosscoders. In *Sparsity in LLMs (SLLM): Deep Dive into Mixture of Experts, Quantization, Hardware, and Inference*, 2025.

Mishra-Sharma, S., Bricken, T., Lindsey, J., Jermyn, A., Marcus, J., Rivoire, K., Olah, C., and Henighan, T. Insights on crosscoder model diffing. *Transformer Circuits Thread*, 2024.

Nanda, N., Chan, L., Lieberum, T., Smith, J., and Steinhardt, J. Progress measures for grokking via mechanistic interpretability. *arXiv preprint arXiv:2301.05217*, 2023.

Olah, C., Mordvintsev, A., and Schubert, L. Feature visualization. *Distill*, 2(11):e7, 2017.

Olah, C., Cammarata, N., Schubert, L., Goh, G., Petrov, M., and Carter, S. Zoom in: An introduction to circuits. *Distill*, 5(3):e00024–001, 2020.

Paulo, G. and Belrose, N. Sparse autoencoders trained on the same data learn different features. *arXiv preprint arXiv:2501.16615*, 2025.

Pham, D. L., Xu, C., and Prince, J. L. Current methods in medical image segmentation. *Annual review of biomedical engineering*, 2(1):315–337, 2000.

Rai, H. M., Yoo, J., and Dashkevych, S. Two-headed uneteficientnets for parallel execution of segmentation and classification of brain tumors: Incorporating postprocessing techniques with connected component labelling. *Journal of Cancer Research and Clinical Oncology*, 150(4):220, 2024.

Rimsky, N., Gabrieli, N., Schulz, J., Tong, M., Hubinger, E., and Turner, A. Steering llama 2 via contrastive activation addition. In *Proceedings of the 62nd Annual Meeting of the Association for Computational Linguistics (Volume 1: Long Papers)*, pp. 15504–15522, 2024.

Ronneberger, O., Fischer, P., and Brox, T. U-net: Convolutional networks for biomedical image segmentation. In *International Conference on Medical image computing and computer-assisted intervention*, pp. 234–241. Springer, 2015.

Rudin, C. Stop explaining black box machine learning models for high stakes decisions and use interpretable models instead. *Nature machine intelligence*, 1(5):206–215, 2019.

Schlemper, J., Oktay, O., Schaap, M., Heinrich, M., Kainz, B., Glocker, B., and Rueckert, D. Attention gated networks: Learning to leverage salient regions in medical images. *Medical image analysis*, 53:197–207, 2019.

Selvaraju, R. R., Cogswell, M., Das, A., Vedantam, R., Parikh, D., and Batra, D. Grad-cam: Visual explanations from deep networks via gradient-based localization. In *Proceedings of the IEEE international conference on computer vision*, pp. 618–626, 2017.

Shinohara, R. T., Sweeney, E. M., Goldsmith, J., Shiee, N., Mateen, F. J., Calabresi, P. A., Jarso, S., Pham, D. L., Reich, D. S., Crainiceanu, C. M., et al. Statistical normalization techniques for magnetic resonance imaging. *NeuroImage: Clinical*, 6:9–19, 2014.

Skean, O., Arefin, M. R., Zhao, D., Patel, N., Naghiyev, J., LeCun, Y., and Shwartz-Ziv, R. Layer by layer: Uncov-
ering hidden representations in language models. *arXiv preprint arXiv:2502.02013*, 2025.

Sultana, F., Sufian, A., and Dutta, P. Evolution of image segmentation using deep convolutional neural network: A survey. *Knowledge-Based Systems*, 201:106062, 2020.

Templeton, A., Conerly, T., Marcus, J., Lindsey, J., et al. Scaling monosemanticity: Extracting interpretable features from claude 3 sonnet. Transformer Circuits Thread, 2024. <https://transformer-circuits.pub/2024/scaling-monosemanticity/index.html>.

Turner, A. M., Thiergart, L., Leech, G., Udell, D., Vazquez, J. J., Mini, U., and MacDiarmid, M. Steering language models with activation engineering. *arXiv preprint arXiv:2308.10248*, 2023.

Wang, M., la Tour, T. D., Watkins, O., Makelov, A., Chi, R. A., Miserendino, S., Wang, J., Rajaram, A., Heidecke, J., Patwardhan, T., et al. Persona features control emergent misalignment. *arXiv preprint arXiv:2506.19823*, 2025.

Xiao, H., Li, L., Liu, Q., Zhu, X., and Zhang, Q. Transform-
ers in medical image segmentation: A review. *Biomedical Signal Processing and Control*, 84:104791, 2023.

Xie, E., Wang, W., Yu, Z., Anandkumar, A., Alvarez, J. M., and Luo, P. Segformer: Simple and efficient design for semantic segmentation with transformers. *Advances in neural information processing systems*, 34:12077–12090, 2021.

Zaigrajew, V., Baniecki, H., and Biecek, P. Interpreting clip with hierarchical sparse autoencoders. *arXiv preprint arXiv:2502.20578*, 2025.

A. Dataset Statistics

We summarize the key statistics of the datasets used in our framework, including domain characteristics, dataset size, and label composition [Table 6](#). We consider both healthy and diseased cohorts. In healthy datasets, segmentation labels correspond to anatomical brain structures such as white matter, gray matter, and cerebrospinal fluid. In contrast, diseased datasets focus on pathological regions, where segmentation targets tumor subregions (e.g., necrotic core, edema, and enhancing tumor).

Table 6. Summary of datasets used in this study

Dataset	Domain	# Volumes	# Classes
IXI	Healthy brain	576	9 (8 subcortical + background)
BraTS Adult	Adult glioma	1,251	4 (3 tumor + background)
BraTS Pediatric	Pediatric glioma	99	4 (3 tumor + background)
BraTS SSA	SSA glioma	60	4 (3 tumor + background)

B. Ablation Studies and Additional Analysis

We present additional ablation studies analyzing the sensitivity of our framework to key design choices. Specifically, we examine the effect of the encoder layer from which activations are extracted and the impact of the SAE expansion factor (dictionary size).

B.1. Effect of Encoder Layer Selection

In the main paper, activations are extracted from a mid-level encoder layer. Here, we assess changes in representation by comparing early-, mid-, and late-stage encoder layers of the SegFormer model trained on the Pediatric cohort.

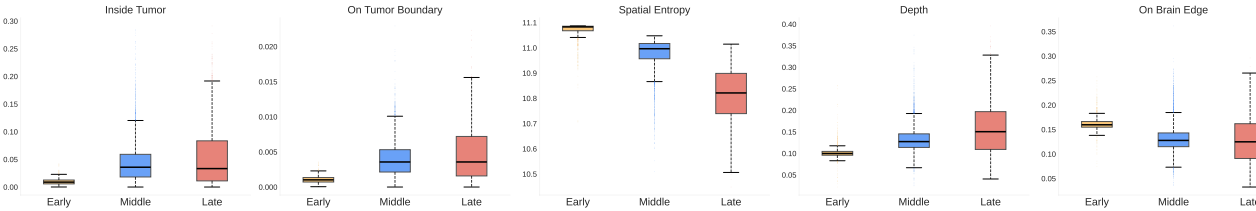


Figure 9. Layer-wise evolution of spatial properties in segmentation representations. SAE latent activations from early, middle, and late layers are compared using geometry-aware metrics.

As shown in [Figure 9](#), geometry-aware metrics exhibit systematic variation across encoder depth. Early-layer latents show low inside-tumor and boundary ratios, together with high spatial entropy and strong alignment with the brain edge, indicating diffuse, globally distributed features that primarily encode coarse anatomical context. In contrast, mid-level representations exhibit increased sensitivity to tumor interiors and boundaries, reduced spatial entropy, and greater activation at intermediate brain depths, consistent with the emergence of localized, task-relevant features. Late-layer latents display the strongest inside-tumor activation and deepest brain localization, accompanied by the lowest entropy, reflecting highly concentrated representations associated with specific anatomical or pathological structures. For consistency and interpretability, we therefore adopt a mid-level encoder block in the main analysis.

[Figure 10](#) provides qualitative examples of SAE latent activations across early, middle, and late encoder layers. Early-layer latents exhibit diffuse, globally distributed activations reflecting coarse anatomical context. Mid-level latents show more structured and localized responses, activating on tumor regions while also capturing surrounding anatomical context, with some features attenuating within tumors and emphasizing non-tumor regions. Late-layer latents are highly localized and strongly aligned with tumor regions, capturing concentrated, task-specific representations. Together, these examples qualitatively mirror the layer-wise trends observed in the geometry-aware metrics.

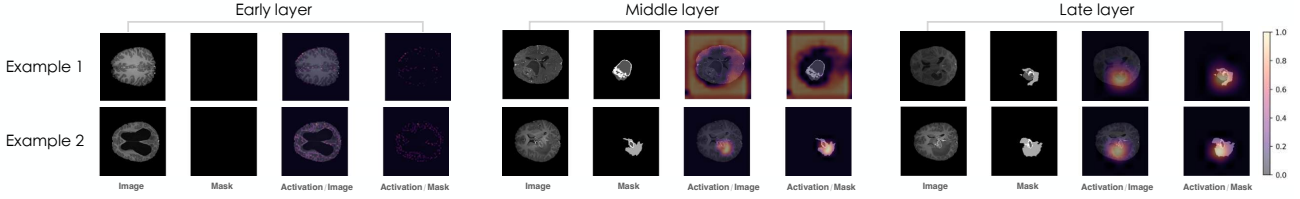


Figure 10. Qualitative comparison of SAE latent activations across encoder layers. As depth increases, latent activations transition from global anatomical patterns to increasingly localized and tumor-specific responses.

B.2. Effect of Dictionary Size

To study the effect of representation capacity, we train SAEs with expansion factors of 8, 16, and 32, corresponding to progressively larger dictionary sizes. Figure 11 summarizes reconstruction quality, explained variance, and sparsity statistics for each setting on the adult dataset. Smaller expansion factors produce broader and less interpretable features, reflecting limited representational capacity and partial feature entanglement. In contrast, larger expansions encourage feature splitting, but at the cost of a substantially higher fraction of dead features, indicating over-parameterization.

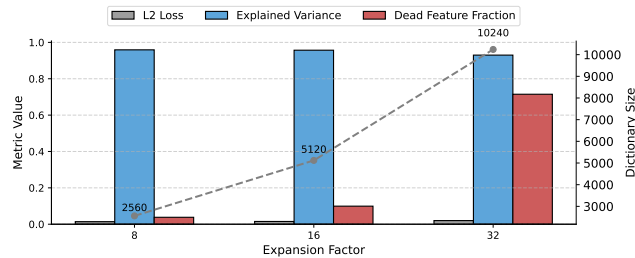


Figure 11. Effect of SAE dictionary size on reconstruction quality and feature sparsity. We evaluate sparse autoencoders trained with expansion factors of 8, 16, and 32, reporting reconstruction error (L2 loss), explained variance, and the fraction of dead features (bars), alongside the corresponding dictionary size (line, right axis). Smaller dictionaries underfit and produce broader, less specific features, while very large dictionaries lead to excessive feature fragmentation and high dead-feature rates. An intermediate expansion factor of 16 provides the best trade-off between reconstruction fidelity and interpretable, active latent features.

Across datasets, an expansion factor of 16 achieves the best balance between reconstruction fidelity, active feature utilization, and semantic interpretability. We therefore adopt this setting in all experiments.

C. Auto-Interpretation Framework: Geometry- and Spatial-Based Metrics

Automated Latent Characterization. For each SAE latent, we analyze its Top- K highest-activating samples and compute the following geometry- and anatomy-aware metrics:

- **Class Association.** Fraction of activation mass assigned to each segmentation class, $p_c = \sum h_{ij} \mathbb{I}[(i, j) \in M_c] / (\sum h_{ij} + \varepsilon)$.
- **Inside and Boundary Sensitivity.** Fraction of activation mass inside labeled regions and along their boundaries, $r_{\text{inside}}, r_{\text{boundary}} = \sum h_{ij} \mathbb{I}[(i, j) \in M, \partial M] / (\sum h_{ij} + \varepsilon)$, where M denotes the anatomical segmentation.
- **Spatial Concentration.** Spatial entropy of the activation map, $\mathcal{H}(h) = -\sum \tilde{h}_{ij} \log(\tilde{h}_{ij} + \varepsilon)$, where lower values indicate localized activations.
- **Brain Edge Preference.** Fraction of activation mass near the brain boundary relative to total mass inside the brain, $r_{\text{edge}} = \sum h_{ij} \mathbb{I}[(i, j) \in E] / \sum h_{ij} \mathbb{I}[(i, j) \in B]$.
- **Brain Depth.** Mean activation-weighted depth from the brain boundary, with values near 0 indicating superficial and values near 1 indicating deep-brain features.

- **Coarse Spatial Localization.** Robust activation centroid estimated from high-activation pixels and expressed relative to the brain extent (left/right, top/bottom, quadrant).
- **Edge Angular Coverage.** Fraction of angular bins around the brain centroid containing high-activation pixels near the brain edge, capturing ring-like versus localized edge responses.

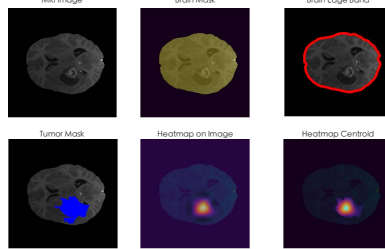


Figure 12. Visualization for some intermediate steps used in auto-interpretation. The top row shows the MRI slice, the extracted brain mask, the cortical edge band used for edge-based measurements. The bottom row illustrates the ground-truth tumor mask, the corresponding latent activation heatmap overlaid on the image, the estimated activation centroid. These spatial and anatomical signals are used to compute geometry-based metrics such as brain edge ratio, brain depth, spatial entropy, and centroid-based localization.

All metrics are computed per image and averaged across Top- K samples, yielding a stable, interpretable descriptor for each latent used in automated semantic labeling and model diffing. Some visualizations of the auto-interp steps are presented in Figure 12.

D. Qualitative Examples of SAE Latents

We present additional examples of SAE latents and their spatial activation patterns. As shown in Figure 13, multiple latents emerge for each tumor or anatomical category, capturing systematic variation in spatial location (e.g., left vs. right), morphology (e.g., diffuse vs. localized), scale, and depth within the brain. These examples demonstrate that SAEs decompose segmentation representations into fine-grained, clinically meaningful features that encode structure beyond mere class presence.

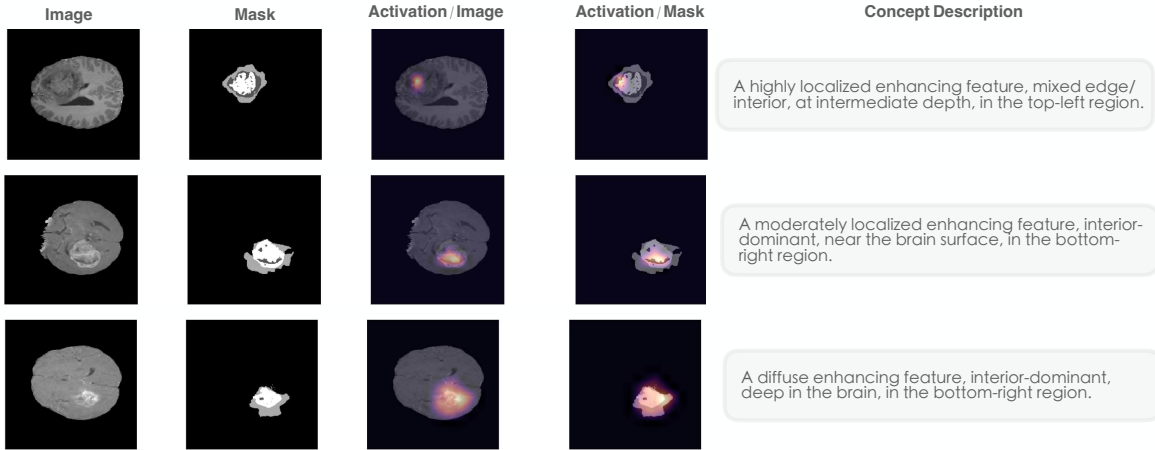


Figure 13. Different SAE latents linked to the same tumor class in the pediatric glioma model, capturing diverse spatial and morphological patterns.

E. Identifying Shared Latents via Model Diffing

Table 7 reports the fraction of shared latents for each dataset pair. All pairs exhibit a non-zero overlap, indicating that models trained on different cohorts learn a partially shared internal basis. The largest overlap is observed between Adult and Pediatric models (58.9%), reflecting their closer anatomical and pathological similarity. Notably, the Adult–Healthy pair

also exhibits a relatively high overlap (36.1%), consistent with both datasets comprising adult brains. In contrast, the overlap is substantially lower for pairs involving the Sub-Saharan African cohort, despite also consisting of adult subjects. This suggests that factors beyond age, such as differences in acquisition protocols, scanners, or imaging conditions, may play a significant role in shaping learned representations, consistent with prior work on MRI acquisition and domain variability (Fortin et al., 2017; Shinohara et al., 2014).

Table 7. Fraction of shared SAE latents between dataset pairs.

	Adult	Pediatrics	Sub-Saharan	Healthy
Adult	–	58.9%	43.2%	36.1%
Pediatrics	58.9%	–	33.9%	28.9%
Sub-Saharan	43.2%	33.9%	–	19.2%
Healthy	36.1%	28.9%	19.2%	–

Feature Swapping. To probe the functional role of shared latents, we perform feature swapping from the Healthy (IXI) model into the Adult glioma model. Specifically, SAE latents identified as shared are replaced with their aligned counterparts from the Healthy model, and their behavior is compared to swaps involving non-shared latents. As shown in Figure 14, swapping shared latents preserves spatial activation structure and anatomical alignment in the Adult model, whereas swapping non-shared latents leads to disrupted or absent activations. These results provide causal evidence that shared latents correspond to transferable internal mechanisms, while non-shared latents capture dataset-specific representations.

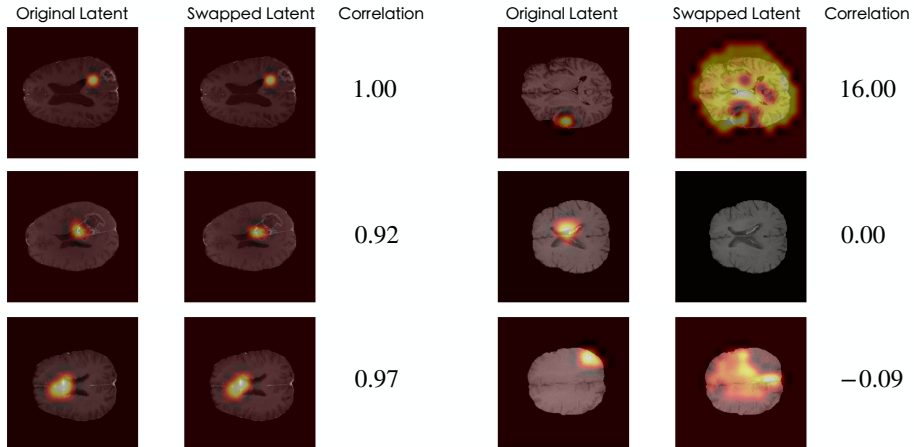


Figure 14. Feature swapping between Adult and Healthy SAEs. Shared latents (left) preserve activation structure and spatial correlation, while non-shared latents (right) produce disrupted or absent activations.

E.1. Details of Alignment Evaluation Metrics

We evaluate latent alignment quality using four unsupervised metrics designed to probe complementary aspects of correspondence without relying on labels or downstream task performance.

Agreement. Agreement measures the fraction of latents for which the encoder-based and decoder-based alignment procedures identify the same matched counterpart. This metric captures internal consistency across representation spaces and tests whether a correspondence is stable under different linear projections of the SAE dictionary.

Stability. Stability evaluates robustness of the alignment under perturbations by repeatedly recomputing matches on bootstrap subsamples of the SAE dictionaries. A latent is considered stable if it is matched to the same counterpart across resampled trials. High stability indicates that the correspondence is not sensitive to small changes in the feature set and reflects a well-conditioned alignment problem.

Collision. Collision measures the rate of many-to-one assignments, where multiple source latents are matched to the same target latent. This metric quantifies ambiguity in the alignment and distinguishes strict bijective matchings from greedy or

soft assignments that allow overlap.

Predictability. Predictability assesses the functional specificity of the alignment by comparing the mean similarity of matched latent pairs against a shuffled baseline. Formally, it measures the gap between aligned similarity and the expected similarity under random pairing. Higher values indicate that the identified correspondences are non-accidental and reflect meaningful shared structure rather than coincidental similarity.

These metrics provide a label-free evaluation of alignment quality, distinguishing surface-level similarity from robust, mechanistically consistent correspondence. We compare alignment quality across Adult–SSA and Adult–IXI dataset pairs, and observe consistent trends across settings, as reported in [Table 8](#).

Table 8. Unsupervised latent alignment comparison across dataset pairs. Agreement and Stability are reported as percentages.

Dataset Pair	Method	Agreement \uparrow	Stability \uparrow	Collision \downarrow	Predictability \uparrow
Adult–SSA	Greedy	97.6	98.9	0.019	72.78
	Sinkhorn	98.5	99.3	0.010	72.72
	Enc-only	98.8	98.6	0.00	72.6
	Ours	100.0	100.0	0.00	88.5
Adult–IXI	Greedy	98.0	98.1	0.018	70.3
	Sinkhorn	98.7	98.9	0.009	70.2
	Enc-only	99.2	99.0	0.00	70.1
	Ours	100.0	100.0	0.00	90.1

F. Non-medical Dataset Validation

To validate the framework applicability beyond medical imaging, we include an additional non-medical semantic segmentation experiment using the CelebAMask-HQ dataset ([Lee et al., 2020](#)). This experiment serves as a lightweight sanity check, assessing whether the proposed latent analysis techniques capture meaningful and reusable structure in a domain with substantially different visual statistics and label semantics.

CelebAMask-HQ is a large-scale face image dataset consisting of 30000 high-resolution images curated from the CelebA dataset following the CelebA-HQ protocol [Table 9](#). Each image is paired with a pixel-wise segmentation mask annotated at a resolution of 512×512 . The dataset contains 19 fine-grained facial-part classes, covering both anatomical components and accessories, including skin, nose, eyes, eyebrows, ears, mouth, lips, hair, hat, eyeglasses, earrings, necklace, neck, and clothing.

Compared to medical imaging datasets, CelebAMask-HQ exhibits higher appearance variability, complex object boundaries, and frequent accessory-induced occlusions. We therefore include it as an additional evaluation setting for applying the same latent analysis pipeline in a non-medical semantic segmentation task.

Table 9. Statistics of the CelebAMask-HQ dataset used for non-medical validation.

Property	Value
Domain	Natural images (faces)
Total images	30,000
Image resolution	512×512
Annotation type	Pixel-wise segmentation
Number of classes	19
Class types	Facial parts and accessories
Example classes	Skin, eyes, nose, mouth, hair, hat, glasses
Primary task	Face parsing / semantic segmentation

Training. We first train a SegFormer model on the corresponding dataset. The model is trained using standard Dice-based segmentation objectives. After training the segmentation model, we extract intermediate activations from fixed encoder

layer and train a BatchTopK Sparse Autoencoder (SAE) on these representations. We use a sparsity level of $k = 32$ and an expansion factor of 16, corresponding to a dictionary size of $16 \times$ the activation dimensionality. These hyperparameters are chosen based on preliminary analysis indicating a favorable trade-off between reconstruction fidelity, sparsity, and feature disentanglement across datasets.

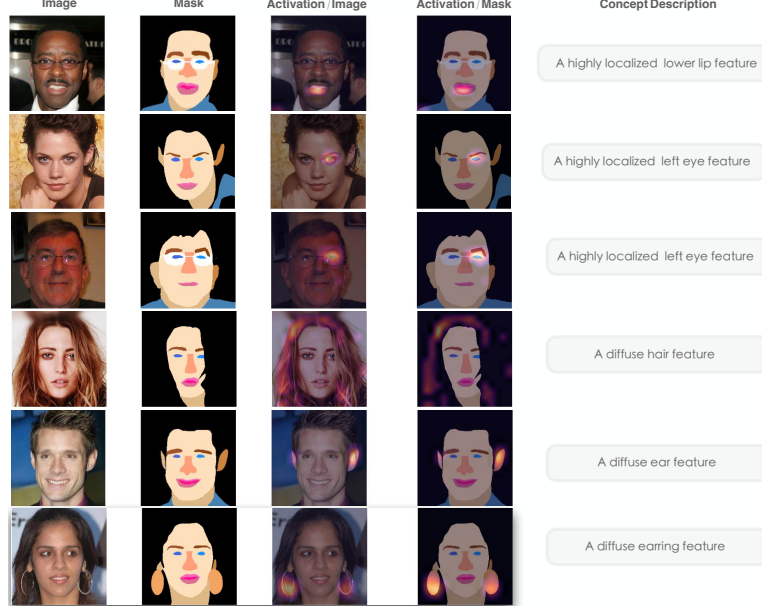


Figure 15. Qualitative examples of automated latent interpretation on the facial-part segmentation task. For each SAE latent, we visualize (from left to right) the input image, the ground-truth segmentation mask, the activation overlaid on the image, and the activation projected onto the mask. The final column provides an auto-generated concept description based on geometry-aware statistics. The results show that individual latents correspond to semantically meaningful facial parts and accessories, ranging from highly localized features (e.g., lower lip, left eye) to more diffuse concepts (e.g., hair, ears, earrings), illustrating both spatial localization and intra-class disentanglement learned by the SAE.

Latent Interpretation. We then apply our automated latent interpretation pipeline to the learned SAE latents, characterizing each feature using geometry-aware statistics such as spatial localization and class association. Qualitative examples of these learned latents and their semantic alignment with facial parts and accessories are shown in Figure 15. Using auto-interp, we observe that many SAE latents align with specific facial components and accessories, and we further find evidence of intra-class disentanglement. For example, the eye class is represented by distinct latents corresponding to subjects wearing glasses versus those without glasses.

Summary. These results provide a qualitative sanity check. They show that the latent analysis and auto-interpretation pipeline can be applied to a non-medical semantic segmentation setting, capturing meaningful and spatially localized concepts.